Unusual Thresholds and Isotope Effects in $Al^+ + H_2/D_2/HD$ Reactions

Richard Bell and Jack Simons*

Chemistry Department University of Utah, Salt Lake City, Utah 84112

Received: October 5, 1998; In Final Form: November 18, 1998

Ab initio quantum chemistry is used to generate a three-dimensional reactive potential-energy surface for the collision of ^1S Al^+ ions with $^1\Sigma_g^+$ H_2 molecules. This surface, in a tessellated and locally interpolated form, is used to generate forces for classical trajectory simulations of the 3.98 eV endothermic $Al^+ + H_2 \rightarrow AlH^+ + H$ reactions with initial conditions appropriate to a thermal H_2 sample and an Al^+ beam of specified center of mass collision kinetic energies in the 3−20 eV range. Our findings indicate that the reaction occurs not on (or near) the collinear path, which has no barrier above the reaction endothermicity, but via a near-C_{2v} insertive path which spontaneously breaks C_{2v} symmetry via second-order Jahn−Teller distortion to permit flux to evolve to $AlH^+ + H$ products. The strong propensity to "avoid" the collinear path and to follow a higher-energy route is caused, at long range, by the ion−quadrupole interaction between Al^+ and H_2 and, at shorter range, by favorable overlap between the H_2 σ_u and Al^+ 3p obitals. Examination of a large number of trajectories shows clearly that reactive collisions (1) lose much of their initial kinetic energy to the repulsive ion−molecule interfragment potential as the closed-shell Al^+ and H_2 approach, (2) transfer significant energy to the H−H stretching coordinate, thus weakening the H−H bond, (3) convert initial H_2 rotational motion as well as Al^+ to H_2 collisional angular momentum into rotational angular momentum of the $HAlH^+$ complex, "locking" the H_2 moiety into the insertive near-C_{2v} geometry about which twisting motion occurs, and (4) allow the Al^+ ion to form a new bond with whichever H atom is nearest it when the system crosses into regions of the energy surface where the H−Al−H asymmetric stretch mode becomes second-order Jahn−Teller unstable, thus allowing fragmentation into $AlH^+ + H$. These findings, combined with considerations of kinematic factors that distinguish among H_2, D_2, and HD, allow us to explain certain unusual threshold and isotope effects seen in the experimental reaction cross-section data on these reactions.

I. Introduction

The reaction of ground-state ^1S Al^+ ions formed with enhanced translational energy in a guided-ion beam source[1] with ground-state, room-temperature H_2 molecules (and isotopic variants) produces AlH^+ ions whose yield is monitored as a function of the kinetic energy of the Al^+ ions. The yield-vs-collision energy data, depicted for H_2, D_2, and HD in parts a−c of Figures 1 as functions of the Al^+ to H_2 center of mass kinetic energy *E*, show several *puzzling features*, the understanding of which forms the focus of the present work:

(1) The thresholds for observation of products all occur at energies considerably in excess of the 3.98 eV endothermicity of the reaction even though there exists a (collinear) reaction path along which no barrier occurs.

(2) The magnitudes of the reactive cross-sections are ca. 2 orders of magnitude below the expected gas−kinetic collision cross-sections of ca. 10^{-16} cm^2.

(3) The thresholds for H_2 and for D_2 are very similar if not identical and are close to that for HD producing $AlH^+ + D$. For HD producing $AlD^+ + H$, the threshold is significantly lower (n.b., these thresholds are not simply related to zero-point energy differences).

(4) The peaks in the cross-sections for H_2, D_2, and AlD^+ from HD occur ca. 2 eV above the corresponding thresholds, but for AlH^+ from HD, the peak occurs ca. 4 eV above its threshold.

Analogous features appear in the experimental data[1] for the $B^+ + H_2 \rightarrow BH^+ + H$ and $Ga^+ + H_2 \rightarrow GaH^+ + H$ reaction cross-sections. We chose to examine the Al^+ case rather than B^+ or Ga^+ because (a) the threshold data for Ga^+ are less accurately known (because they are more challenging to measure) for the H_2, D_2, and HD isotopes, and (b) although the experimental data are well-known for B^+, the magnitudes of the threshold shifts among the H_2, D_2, and HD isotopes is smaller than in the Al^+ case, a result of which our computations would have to be carried out at a much higher level of theory to be reliable enough to address such differences (this was simply not computationally feasible). On the other hand, we believed that the threshold differences and reaction cross-section magnitudes for Al^+ were sufficiently pronounced to allow us to perform standard (i.e., not using extremely large atomic-orbital basis sets and not employing high-level treatments of dynamical electron correlation) ab initio methods to compute, at thousands of geometries, a three-dimensional surface for the Al^+ reactions and to thereby contribute to understanding the unusual threshold effects.

This reaction was previously studied by Gutowski and co-workers,[2] who proposed a viable process by which this reaction could take place consistent with the range of kinetic-energy thresholds observed experimentally. It was proposed that this reaction most likely takes place via C_{2v} symmetry. Their results were analogous to previous findings for theoretical studies on[3] the systems $Be(^1S) + H_2 \rightarrow HBeH(^1\Sigma_g^+)$ and on[4] $B^+(^1S) + H_2 \rightarrow HBH^+ (^1\Sigma_g^+)$, $BH^+(X^2\Sigma^+) + H(^2S)$. They also speculated that the rate-limiting step in these reactions is the transfer of collision energy to the internal vibrational energy of the H−H′ diatomic molecule, which then causes the diatomic bond to lengthen and eventually rupture, allowing the reaction to ensue.

10.1021/jp983966u CCC: $18.00
Published on Web 01/09/1999

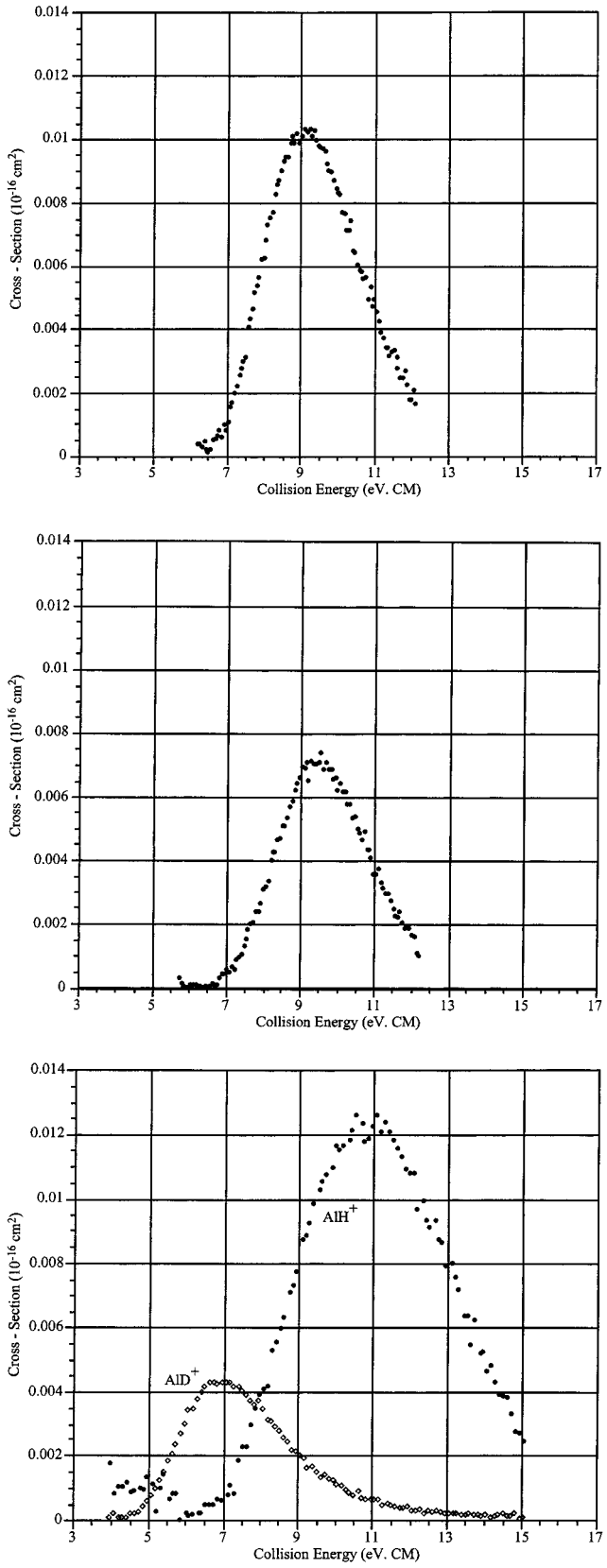

Figure 1. Shown are the experimentally determined cross-sections versus center of mass collision energy for (a) $Al^+ + H_2$, (b) $Al^+ + D_2$, and (c) $Al^+ + HD$ from ref 1. The cross-sections are in cm^2, and the collision energies are in eV.

They determined that the collision energy required to reach geometries where dynamical resonances occur were consistent with the experimentally observed reaction thresholds. Chacon-Taylor and Simons[5] focused their efforts on quantifying the work of Gutowski[2] employing classical trajectories as a means to study the collision-to-vibrational energy transfer step. However, those classical trajectory simulations were unable to shed light on the nature of the isotope effects mentioned above.

In this work, we focused our attention on a more rigorous approach, still using classical trajectories, in an effort to characterize this reaction. Specifically, we decided to extend the classical trajectory approach by employing a realistic ab initio potential-energy surface rather than the kind of model surface used in ref 5. We combined our two-dimensional (the H−H distance r and the Al^+ to H−H midpoint R) ab initio C_{2v} $^1A_1$ ground-state electronic potential-energy surface with an analytical potential function describing the bending (or asymmetric stretching) in terms of ab initio calculated force constants. The method applied in this work uses the ab initio energy and gradients at any geometry to interpolate, using only data at neighboring points. The set of ab initio data is calculated only once; then an interpolant continuous through the first derivative is used to generate the gradients at arbitrary geometries for use in trajectory propagation.

As a result of employing the tools briefly outlined above, we are able to present the results of our ab initio calculation of the three-dimensional $Al^+ + H_2 \rightarrow AlH^+ + H$ ground-state energy surface and our subsequent classical trajectory investigation of the fate of collisions on this surface. Our findings display the same kind of unusual threshold and isotope effects described above. Analysis of the reactive trajectories suggests a physical explanation of these effects in terms of the forces operative on the reaction surface.

II. Methods Used

A. Electronic Structure Calculations. *1. Atomic-Orbital Basis Sets.* For the H-atom basis set[6] we employed a modified Dunning-augmented correlation consistent (cc) polarized valance triple-ζ (p-VTZ) (5s2p1d|3s2p1d) basis but without the 1d orbitals (our earlier work[2] justified excluding these d orbitals). For the Al^+ ion, the McLean-Chandler[7] (12s9p|6s5p) basis set was used. In all, a total of 39 contracted Gaussian basis functions were included in generating the potential-energy surfaces at the multitude of geometries detailed later. Although this basis is quite modest in size, it was shown in ref 2 to be capable of duplicating the thermochemistry of the reaction and the essential features of the reactive energy surface.

2. Treatment of Electron Correlation. The complete active space (CAS) based multiconfigurational self-consistent field (MCSCF) method was used to construct the $^1A_1$ ground-state potential-energy surface as well as the excited $^1B_2$ and $^3B_2$ surfaces. We had to examine the latter two surfaces to consider the possibilities of second-order Jahn−Teller couplings and of surface hoppings (in the dynamics). The MCSCF calculations of the potential-energy surfaces were accomplished using the electronic structure program GAMESS.[8] As discussed in ref 2, the motivation for using the multiconfigurational approach is based in considering how the closed-shell $3s^2$ configuration of Al^+ and the σ_g^2 configuration of $X^1\Sigma_g^+$ H_2 evolves into the $\sigma_g^2\sigma_u^2$ configuration of the $HAlH^+$ molecule (that lies in a deep well on the $^1A_1$ surface) and the σ^2 σ^1 $1s^1$ configuration of the $AlH^+ + H$ products.

To test our basis set and method for treating electron correlation, we used this same MCSCF level of theory to calculate the electronic state energies for ^3P (Al^+) and ca. 4.6 eV and for ^1P (Al^+) at ca. 8.4 eV as well as the endothermicity for $Al^+(^1S) + H_2(^1\Sigma_g^+) \rightarrow AlH^+(^2\Sigma^+) + H$ at ca. 3.98 eV. These

results for ^{3}P and ^{1}P can be compared to the experimental values of 4.64 and 7.42 eV, respectively,[9] and our reaction endothermicity is close to the experimental value of ca. 3.8 eV.[1]

B. Surface Tessellation and Interpolation. The tessellation and interpolation methodology developed earlier[10] has been used to generate a local piecewise description of the $^1A_1$ potential-energy surface (PES) in a form especially useful for classical trajectory propagation because the forces, computed as gradients of the PES, are continuous within each local region and across neighboring regions. There are three ingredients to this scheme: (1) tessellation of the coordinate space used to describe the reacting species, (2) interpolation of the energy (and its derivatives) within and across local tessellated regions, and (3) approximation of energy gradients at the points where energies are known but analytical gradients are not available.

1. Tessellation of the Energy Surface. We use two internal coordinates (r and R defined above), the domain of which we divide into simplices, and a third coordinate (the asymmetric stretch distortion) whose influence on the PES we represent in the analytical form discussed below. In two-dimensions (2D), the simplices are triangles. Any given 2D domain will admit to many different triangulations, so an optimum triangulation[11] is used which attempts to minimize the number of triangles with one very small internal angle, because such regions cover little area and decrease the accuracy of the interpolant. One convenient method of facilitating this, as put forth in ref 10, involves tessellating with barycentric coordinates and employing a so-called sphere test to distinguish between competing triangulations. The barycentric coordinates (b_i) of a point x_4,y_4 within a 2D domain are computed by solving the following set of linear equations:

$$\begin{bmatrix} 1 & 1 & 1 \\ x_1 & x_2 & x_3 \\ y_1 & y_2 & y_3 \end{bmatrix} \begin{bmatrix} b_1 \\ b_2 \\ b_3 \end{bmatrix} = \begin{bmatrix} 1 \\ x_4 \\ y_4 \end{bmatrix} \tag{1}$$

where the x_i's and y_i's ($i = 1, 2, 3$) are the x and y coordinates of the three vertices of the triangle that make up the domain of the 2D surface.

2. Interpolation of the Energy within and across Regions. Given the tessellated domain of the PES (i.e., a set of vertexes or node points $\{r_i,R_i\}$ as well as knowledge about which triangles these points lie on), along with the energies $\{E_i\}$ and gradients $\{\mathbf{g}_i\}$ at the nodes of this tessellated PES, one may interpolate the energy and gradients anywhere within the domain. The energy and gradient interpolation used in the present work is the Clough−Tocher interpolant[12] (CT). The CT interpolant expresses the energy E at a point $p = (r,R)$ within any particular triangle in terms of the barycentric coordinates $\{b_i\}$ of that point determined as described above:

$$E(P) = \sum_{i+j+k+l=3} \frac{3!}{i!j!k!l!} c_{ijkl} b_1^i b_2^j b_3^k b_4^l \tag{2}$$

The particular choice of the coefficients $\{c_{i,j,k,l}\}$ given in ref 10 that defines the CT interpolant insures the continuity of the energy and its gradients within any triangle and across the boundaries of neighboring triangles, and therefore total energy and momentum will be conserved when such an interpolant is employed.

3. Node Gradient Approximation if Analytical Gradients Are Not Available. Since the CT interpolant necessitates knowing the energies *and gradients* at each triangle node and because it is quite possible that one will not have access to the ab initio gradients at all such points, a method for generating approximate gradients at the nodes is needed. The hyperbolic multiquadric method (MUL) has been shown to be particularly useful[9] in this endeavor. The 2D MUL approximates the energy E_j at a point (r_j,R_j) as

$$E_j(r_j,R_j) = \sum_{i=1}^{K} c_i \sqrt{d_{ji}^2(r_{j,i},R_{j,i}) + \epsilon} \tag{3}$$

where

$$d_{ji}^{\ 2}(r_{j,i},R_{j,i}) = (r_j - r_i)^2 + (R_j - R_i)^2$$

is the square of the distance from the point (r_j, R_j) where the energy is needed to the point (r_i, R_i) where the energy is known and ϵ is a "range parameter" that controls the distance over which data influences the approximation (see ref 10 for further discussion). The set of coefficients $\{c_i\}$ are determined by using eq 3 at the K nearest-nodal points $\{r_k,R_k\}$, where the energies E_k are known and solving the $K \times K$ set of linear equations:

$$\begin{bmatrix} \sqrt{d_{11}^{\ 2} + \epsilon} & \cdots & \sqrt{d_{1k}^{\ 2} + \epsilon} \\ \vdots & \ddots & \vdots \\ \sqrt{d_{k1}^{\ 2} + \epsilon} & \cdots & \sqrt{d_{kk}^{\ 2} + \epsilon} \end{bmatrix} \begin{bmatrix} c_1 \\ \vdots \\ c_k \end{bmatrix} = \begin{bmatrix} E_1 \\ \vdots \\ E_k \end{bmatrix} \tag{4}$$

The resultant set of coefficients $\{c_k\}$ are then substituted back into eq 3. Then by differentiating eq 3, one obtains expressions for the desired gradients to evaluate $\partial E/\partial r$ and $\partial E/\partial R$ at the node (r_j,R_j) thus supplying the needed gradient information for the CT interpolant. The process is repeated for all of the nodes in the domain.

Figure 2 shows a contour plot of the resultant $^1A_1$ PES where the tessellation, interpolation, and gradient generating methods described above have been applied in this work. The domain of the PES shown in Figure 2 was divided into 2400 triangles.

C. Classical Trajectory Simulations. *1. Coordinate System.* Figure 3 displays two different sets of coordinates. The first are the internal coordinates mentioned above that are used to construct the $^1A_1$ potential-energy surface, $V(R,r,\theta)$. R is the magnitude of the vector **R** connecting the Al^+ ion to the *center* of the hydrogenic diatomic, r is the length of the vector connecting H to H′, and θ is the angle between the vectors **R** and **r**. To follow the classical trajectory dynamics, it is useful to use coordinates in which the kinetic energy does not contain cross terms. These Jacobi coordinates are the Al^+ to *center of mass* of H−H′ distance R', the same r coordinate, and the angle θ' between the **r** and **R′** vectors. Of course, $R = R'$ and $\theta = \theta'$ if H = H′. The angles α and β give the polar coordinates of **R′** and **r**, respectively, in a space-fixed coordinate system. Finally, the angle θ' between **R′** and **r** is related to α and β by $\theta' = \alpha + \beta$. The trajectory simulations used here involve motions in which the plane of $AlHH'^+$ is assumed not to deviate from its initial orientation in space; that is, our trajectories assume that Coriolis forces associated with tumbling of the plane of the $AlHH'^+$ ion are unimportant.

The time evolution of the angle coordinates α and β are not independent since the z-component (i.e., the out of plane component) of the angular momentum

$$L_z = \tilde{m}R'^2\dot{\alpha} - \mu r^2\dot{\beta} = p_\alpha - p_\beta$$

is a conserved quantity. Here, $\tilde{m} = m_{Al}(m_H + m_{H'})/(m_{Al} + m_H + m_{H'})$ and $\mu = m_H m_{H'}/(m_H + m_{H'})$. Hence, it is possible to

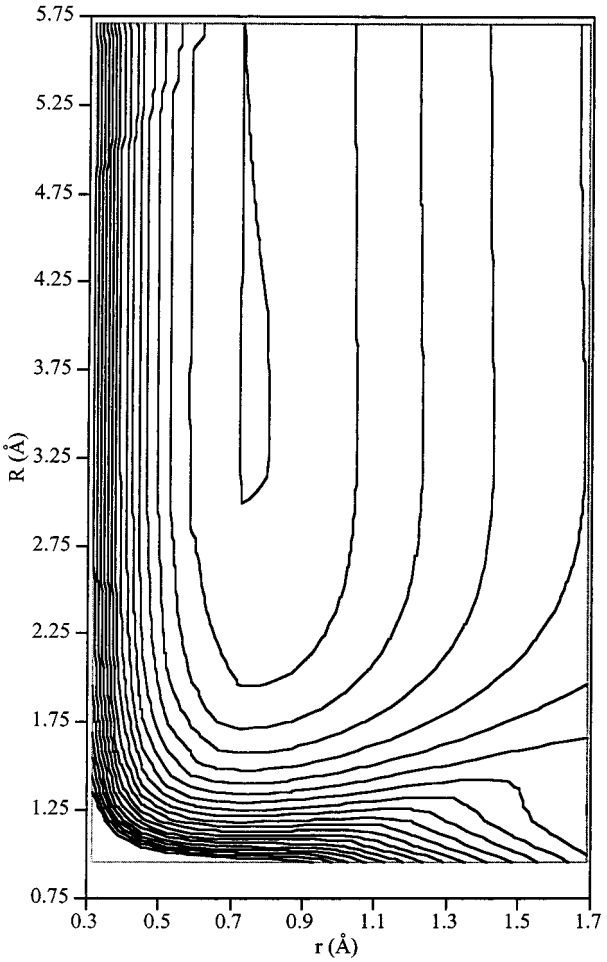

Figure 2. C_{2v} symmetry contour plot of the $^1A_1$ ground-state potential-energy surface of $Al^+ + H_2$. The R axis is the distance from Al^+ to the center of the H_2 bond in Å, and the r axis is the H_2 bond distance in Å. The contours are spaced by 0.75 eV.

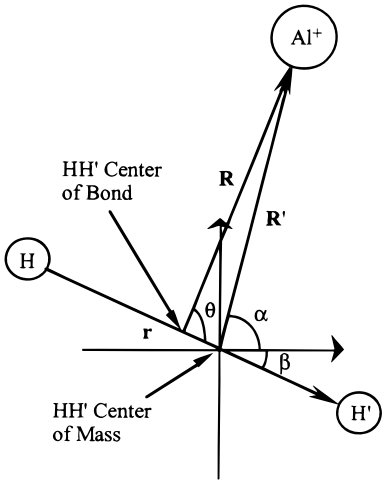

Figure 3. Jacobi and internal coordinates for the three-atom system. The Jacobi coordinates are denoted by the vectors **R**′, **r**, and the angle between them is $\theta' = \alpha + \beta$. The internal coordinates are the vectors **R**, **r** and the angle θ between them. For m_H = to $m_{H'}$, the Jacobi and internal coordinates are indistinguishable.

express the dynamics in terms of a Hamiltonian

$$H = \frac{p_{R'}^2}{2\tilde{m}} + \frac{p_r^2}{2\mu} + \frac{p_\alpha^2}{2\tilde{m}R'^2} + \frac{p_\beta^2}{2\mu r^2} + V \qquad (5)$$

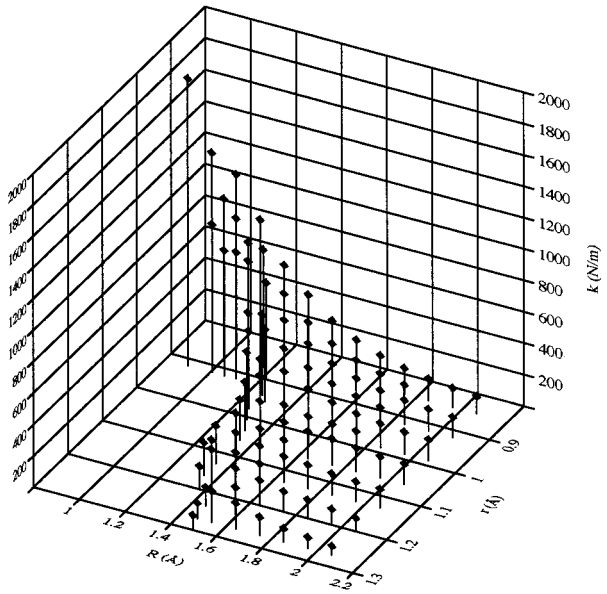

Figure 4. Three-dimensional plot of the R, r coordinates for C_{2v} symmetry and their corresponding force constants calculated from eq 7 along the entrance channel up to the seam c of Figure 7 denoted by the dashed line representing where the force constant becomes zero.

that determines the time evolution of four coordinates (R', r, α, and β) and three momenta ($p_{R'}$, p_r, and p_β).

In our simulations, we propagated trajectories in Cartesian coordinates (where we verified energy and angular momentum conservation), although we expressed the tessellated energy surfaces in terms of the above internal coordinates and converted all forces from internal to Cartesian coordinates. We convinced ourselves (for details, see section III.A), by carrying out ab initio calcualtions at a wide range of orientation angles θ, that the $Al^+ - H_2$ entrance channel surface is (a) negatively curved (i.e., repulsive) near collinear geometries (near $\theta = 0°$, 180°) and (b) positively curved at insertive geometries (near $\theta = 90°$, 270°). These observations motivated us to model the θ-dependence of the PES, accounting for the twisting motion of the diatomic relative to Al^+, in the following analytical form

$$V(R,r,\theta) = V_{\text{less}}(R,r) + \frac{1}{4}k(R,r)(r_{\text{Al-H}} - r_{\text{Al-H}'})^2 \qquad (6)$$

where V_{tess} is the potential obtained from the tessellated and interpolated surface detailed earlier and $r_{\text{Al-H}}$ and $r_{\text{Al-H}'}$ are the distances from Al^+ to the H and H′ atoms, respectively. We performed ab initio Hessian calculations for many values of R and r within the entrance channel in order to find the local b_2 vibrational frequencies associated with each such point. The twisting force constant at each point was calculated using the relationship

$$k(R,r) = \frac{\lambda_{b_2}(R,r)}{\frac{1}{m_H} + \frac{1}{m_{Al}}(1 - \cos(\gamma))} \qquad (7)$$

where and γ is the angle between $r_{\text{Al-H}}$ and $r_{\text{Al-H}'}$ and λ_{b_2} is the square of the b_2 mode frequency. The resulting values of these twisting force constants $k(R,r)$ were then tessellated in the same manner as the energy. Shown in Figure 4 are the force constants k and the associated values of the R, r coordinates. It is important to note that k is small for large R (nor surprisingly) but becomes quite large as R decreases. However, there is a region beginning near $R = 1.5$ Å and $r = 1.3$ Å where k drops

sharply to zero (where the vertical "sticks" cease to appear) because of second-order Jahn−Teller coupling with a nearby $^1B_2$ state. This region will play a central role in the dynamics as will be seen shortly.

2. Initial Conditions. a. Linear Coordinates, Momenta, and Weights. The initial Jacobi distance R' of the Al^+ ion from the center of mass of the hydrogenic diatomic was taken to be ca. 5.3 Å in all trajectories (this is large enough to be in the asymptotic region as seen in Figure 2). The initial relative momentum p_R (always negative to simulate a collision) of the Al^+ and diatomic reactant was obtained by scanning the collision energy range from 3 to 20 eV incrementally.

Since the temperature of the HH′ gas in the experiment was maintained at 305 K, the only vibrational level readily accessible is $v = 0$. The initial distance r was sampled over a range between the inner and outer turning points for the diatom in its $v = 0$ vibrational level with a weighting factor[13a] of $|\Psi_{v=0}(r)|^2\Delta r$. The initial vibrational momentum p_r of the diatom was then determined by using the bond length r and conservation of energy

$$\frac{p_r^2}{2\mu} + V_{HH}(r) = E_{v=0} \tag{8}$$

where V_{HH} and $E_{v=0}$ are the (Morse approximation to the) potential and vibrational energy, respectively. Except at the turning points, both positive and negative values for p_r were selected, with a separate trajectory run for each case.

b. Impact Parameter, Angular Coordinates, Momenta, and Weights. The impact parameter b was varied from 0.1 to 0.7 Å in uniform increments of 0.2 Å with a weighting factor[13b] of $2b/b_m^2$ for $b \le b_m$ and zero for $b > b_m$; the maximum impact parameter $b_m = 0.7$ Å was determined by examining when the reaction probability decreased sufficiently to ignore larger b values. The Al^+ ion's angular coordinate α was computed from $\cos(\alpha) = b/R'$. Each b value produces $\tilde{m}\dot{R}'b$ in collisional angular momentum as a contribution to the total initial angular momentum. The velocity corresponding to the angle α is computed as $\dot{\alpha} = (\dot{R}'b)/R'^2$.

The initial value of the hydrogen diatom's phase angle β was systematically varied from 0 to $\pi/2$ for H_2 and D_2 and from 0 to π for HD in units of $\pi/12$ rad (these limiting values of the angle β were chosen to avoid redundant simulations). The initial rotational angular velocity was obtained from the angular momentum of the hydrogen diatom $(\mu r^2\dot{\beta}) = \sqrt{J(J+1)}\hbar$ for the diatom in $J = 0$, 1, and 2 (for H_2) and $J = 0$, 1, 2, and 3 (for HD and D_2) and was allowed to take on both positive and negative projections along the axis perpendicular to the molecular plane. The weight associated with the rotational state was proportional to $(2J + 1)\exp((-BJ(J+1))/kT)$.

On the basis of the above sampling scheme, at *each* collision energy, we carried out an ensemble of 23 688 trajectories for HD, 12 852 for H_2, and 10 332 for D_2. Although our methods for choosing initial conditions for our trajectories may not be as efficient as, for example, Monte Carlo sampling or more sophisticated means of discretizing and sampling the ranges of coordinates and momenta values, because we use so many trajectories and because they are, in principle, correct, our final results can be trusted.

3. Tabulation of Reaction Cross-Section. The reaction cross section for each collision energy is determined by the expression

$$\sigma = \frac{\sum_{i=1}^{N} w_i \pi b^2 \Omega}{\sum_{i=1}^{N} w_i} \tag{9}$$

where w_i is the product of the weights discussed above, which produces the unnormalized weight of the ith trajectory, b is the impact parameter, Ω is 1 for a successful trajectory and 0 for an unsuccessful trajectory, and N is the total number of trajectories for a given collision energy. The denominator is the sum of all the unnormalized weights whether a trajectory is successful or not and is used to normalize.

III. Findings

A. The Potential-Energy Surface. *1. The Collinear Approach is Not Operative.* Along a path preserving collinear geometry, the $Al^+ + H_2 \rightarrow AlH^+ + H$ reaction is symmetry allowed yet endothermic by ca. 3.98 eV. The $(3s^2\sigma_g^2)\ ^1\Sigma^+$ orbital and state symmetries of the reactants correlate directly with the $(\sigma^2_{AlH}\sigma^1_{Al}1s^1_H)\ ^1\Sigma^+$ orbital and state symmetries of products. Indeed, we find an energy profile along this path that rises monotonically from $Al^+ + H_2$ to $AlH^+ + H$ as shown in Figure 5.

However, along this collinear path, the ab initio calcualtions that we carried out (discussed in section II.C.1) clearly show a force field along the bending degrees of freedom that causes trajectories to move away from collinear geometries. To illustrate, in Figure 6, we show our ab initio energies for various values of R and θ (r is held fixed at the equilibrium bond length of 0.7557 Å) at geometries describing Al^+ approaching H_2 in a collinear manner. Clearly, at large R, the potential energy is nearly independent of θ, thus allowing for free rotation of the H_2 molecule. However, as R decreases, the shape of the energy surface along the θ coordinate produces a stronger and stronger tendency to direct flux away from $\theta = 0$ (or $\theta = \pi$) toward $\theta = \pi/2$. These ab initio findings guided us in developing the twisting potential form used in our entrance-channel dynamics (see section II.C.1). We stress that the energy surface's negative curvature near $\theta = 0$ and positive curvature near $\theta = \pi/2$ is a result of our examining the surface using ab initio methods rather than a postulate of our model. Given these facts about the angle-dependence of the surface, we then designed the functional form shown in eq 6 to represent this behavior.

The origin of the strong negative curvature along θ lies not in the symmetries of the reactant and product molecular orbitals (i.e., it is not a Woodward−Hoffmann effect), but in the *electrostatic interactions* of the positive Al^+ ion with the H_2 molecule. At long range, these interactions are characterized by the potential

$$V = \frac{qe}{4R^3}(3\cos^2\theta - 1) - \left[\frac{\alpha_{\parallel}e}{2R^4}\cos^2\theta + \frac{\alpha_{\perp}e}{2R^4}\sin^2\theta\right] \tag{10}$$

The first term is the potential due to the quadrupole moment of H_2. The last two terms are the potential due to the polarizabilities of H_2, where $\alpha_{\parallel}$ is the polarizability of H_2 along the axis of the molecule and $\alpha_{\perp}$ is the polarizability of H_2 perpendicular to the H_2 bond axis. As R decreases, the interaction between Al^+ and the *quadrupole moment* of H_2 becomes strong enough to dominate the θ-dependence of the energy surface (the charge-induced-dipole interaction is not strongly θ-dependent because

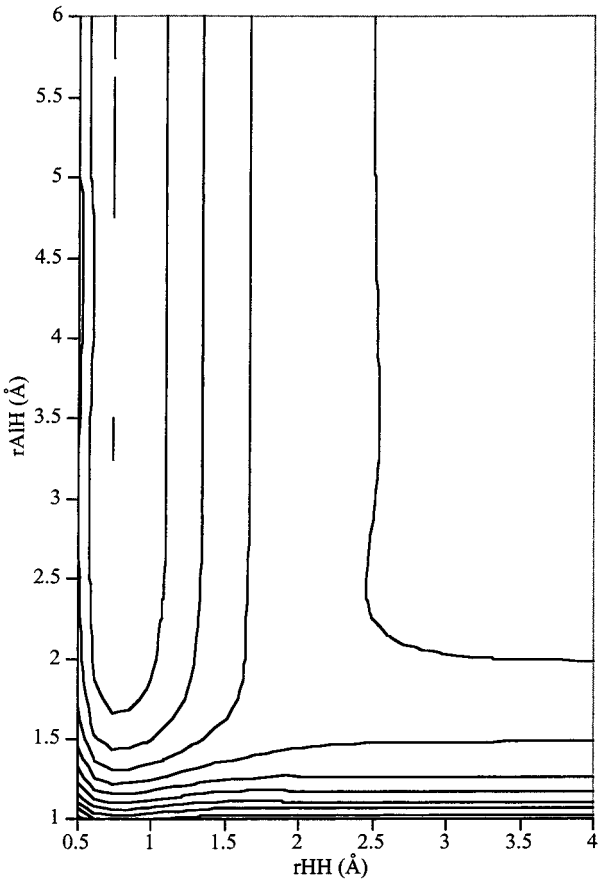

Figure 5. Collinear $Al^+ + H_2$ contour plot of the ground-state potential-energy surface. The r_{AlH} axis is the distance from Al^+ to the end of the H_2 diatomic in Å, and the r_{HH} axis is the H_2 distance in Å. The contours are spaced by 1.0 eV.

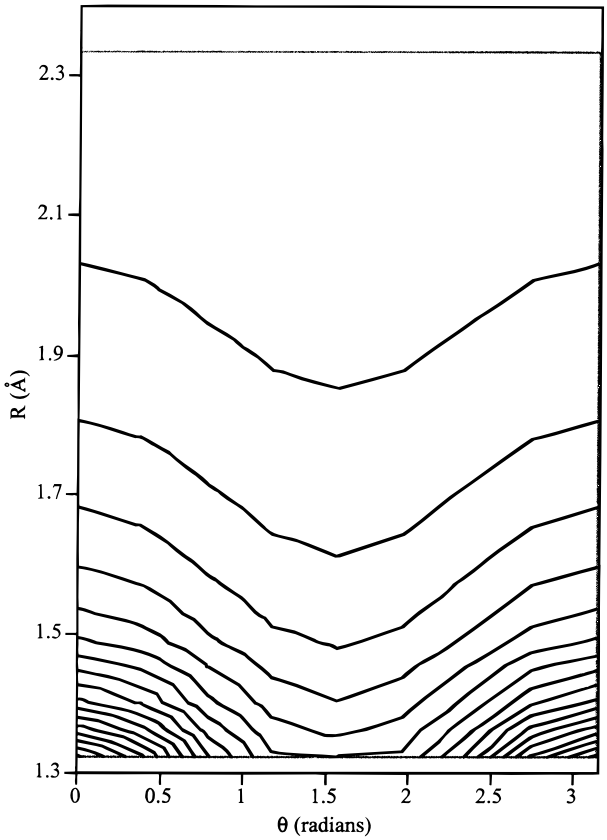

Figure 6. Contour plot of the ground-state PES as a function of the Al^+ to the center of H_2 distance and the angle θ between **R** and the H_2 bond axis. The H_2 distance has been held fixed near the equilibrium bond length 0.7557 Å. The contours are spaced by 1.0 eV.

the polarizability of H_2 is only slightly anisotropic). The *charge−quadrupole interaction* has a maximum at $\theta = 0°$ (and at multiples of π) and a minimum at $\theta = 90°$ (and at 90° plus multiples of π). Because H_2 has a quadrupole moment with its negative portions focused near the H−H bond midpoint and with its positive portions focused near the H nuclei, this component of the ion−molecule potential favors C_{2v} geometries over collinear geometries. At even smaller R values, it is the overlap of the H_2 molecule's σ_g orbital with the "sideways" 3p orbital of Al^+ that strongly favors insertive C_{2v} geometries.

Therefore, as a result of the charge−quadrupole and σ_g−3p orbital interactions, trajectories move away from collinear geometries and spend the majority of their time (once the Al^+−H_2 interaction becomes strong enough to alter the rotation of the H_2 moiety) *near* C_{2v} geometries (of course, oscillatory excursions away from C_{2v} symmetry still occur). Moreover, the volume element associated with the initial conditions also contributes to the dominance of insertive paths over near-collinear paths. Thus, the reactions between Al^+ and H_2 are dominated by collisions that do not follow the collinear path (the collinear path evolves into a ridge that flux falls away from (see Figure 6)) but, instead, follow "insertive" paths.

2. The PES Along the Insertive Path. The near-C_{2v} portion of the energy surface depicted in Figure 2 shows a narrow channel beginning at large R and leading inward. Along this channel, the surface becomes more and more repulsive as R decreases and the θ-dependence of the potential (not shown) displays the characteristic shape discussed above with a minimum at C_{2v} geometries and a maximum at collinear geometries (see Figure 6 and recall that the energies shown were obtained from our ab initio data).

However, a qualitative change occurs rather suddenly (n.b., this change is related to the sudden change in the asymmetric stretch force constants shown in Figure 4) in the surface's angle dependence as the "seam" region denoted by *c* in the close-up view of the C_{2v} surface shown in Figure 7 is reached. Prior to the seam, the positive curvature along θ forces flux to maintain near-C_{2v} geometries. Once the seam is crossed, the H−Al−H^+ ion's twisting (or asymmetric stretching) mode becomes unstable (i.e., the curvature along this direction becomes negative); as a result, flux is free of the forces that maintain near-C_{2v} symmetry, thus allowing it to progress onward to $AlH^+ + H$ products.

The physical reason underlying the change in the twisting mode's curvature from positive to negative is that as one approaches and crosses the seam, an excited electronic state of $^1B_2$ symmetry (deriving from the ^1P excited state of Al^+) lies slightly above the $^1A_1$ state. The relative energies of our $^1A_1$ reactive PES and the nearest singlet (and corresponding triplet) states are shown in Figure 8 along the path marked a in Figure 7. Near the seam, the $^1B_2$ state is close enough to our $^1A_1$ (in C_{2v}) or $^1A'$ (in C_s) ground state to undergo *second-order Jahn−Teller coupling* with our state along the bending coordinate (which has b_2 symmetry) in a manner that induces negative curvature along θ.[14,15] The factors that give negative curvature along the b_2 mode are controlled by matrix elements[16] of the form

$$\frac{|\langle {}^1A_1|\partial H/\partial Q_{b2}|{}^1B_2\rangle|^2}{E({}^1A_1) - E({}^1B_2)} \qquad (11)$$

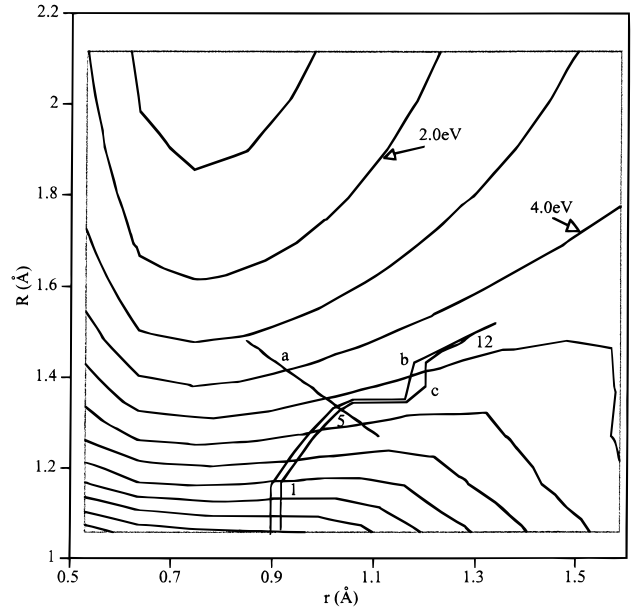

Figure 7. Close up of the C_{2v} symmetry contour plot shown in Figure 2 of the region where the b_2 vibrational mode becomes unstable. The line marked a is used to scan the $^1A_1$, $^1B_2$, and $^3B_2$ potential-energy surfaces (see Figure 8). The seam marked c denotes where the force-constant surface shown in Figure 4 drops to zero. Seam b is where we halt trajectories while the force constant is still nonzero (see section III.A.4).

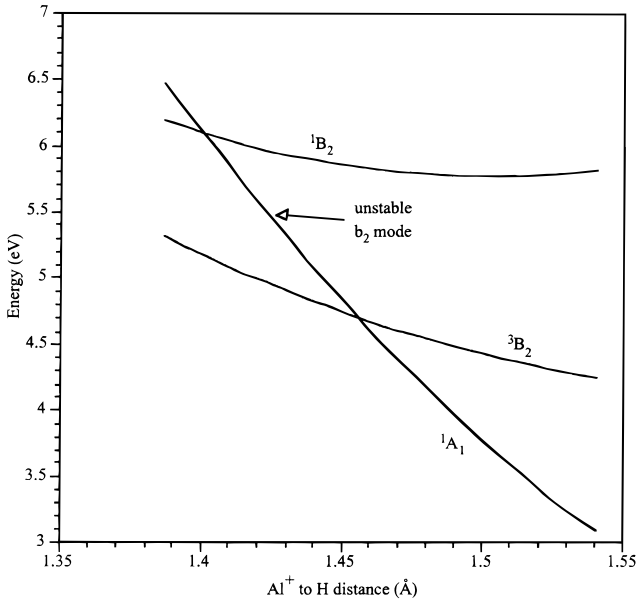

Figure 8. Slices through the $^1A_1$, $^1B_2$, and $^3B_2$ surfaces along the line marked a in Figure 7. The ordinate is the potential energy in eV, and the abscissa is the Al^+ to H distance in Å of the diatomic in C_{2v} symmetry.

where $\partial H/\partial Q_{b2}$ is the derivative of the electronic Hamiltonian with respect to changes along the b_2 mode. It is also near this seam that concerted breaking of the H−H′ bond and formation of the new Al−H bond occur.

We conclude, therefore, that *trajectories must access the seam* on the energy surface near which the twisting mode becomes unstable if they are to become reactive trajectories. At various collision energies, this seam is accessed at different regions, but only at collision energies above ca. 5 eV (i.e., the lowest energy point on the seam) can trajectories react. In other words, *for collisions with energies above the thermodynamic threshold of 3.98 eV but below 5 eV, the seam region is inaccessible, so reaction cannot take place*.

Before moving on to analyze the results of our classical trajectory simulations on the PES discussed above, we wish to emphasize that the qualitative features of the PES discussed above, in our opinion, would be difficult to model using simple pairwise-additive interatomic potentials. In particular, the rather *sudden* change in the θ-dependence, induced by coupling with the low-lying $^1B_2$ state, as well as the change in electronic structure from one involving an intact H−H′ bond plus a closed-shell Al^+ ion to one describing a $^2\Sigma$ AlH^+ ion and a H′ atom would be difficult to model.

3. The PES After the Seam Region is Crossed. Knowing that the reactive PES becomes unstable to asymmetric distortions upon crossing seam c in Figure 7, a strategy for characterizing the evolution of trajectories as fragmentation to $AlH^+ + H'$ products remained to be developed. Our primary interests in this study were to determine (a) whether each trajectory would "react" to produce a nascent AlH^+ or AlD^+ product and (b) whether the newly born molecular-ion product would remain bound or have so much internal energy that it would dissociate before reaching the detector. We used the crossing the seam region on the reactive PES to define that a trajectory can create a nascent molecular ion. However, we still needed to develop a method to determine whether this ion would dissociate or remain bound. Clearly, we could have computed (at thousands of points) the PES on the exit channel (i.e., as the distance between the departing H′ atom and the AlH^+ ion increases) as functions of three coordinates describing the $AlH^+ + H'$ species. After doing so, we could have tessellated and interpolated this surface and carried out classical trajectory simulations following the $AlH^+ + H'$ evolution until the H′ became distant enough to interrogate the internal energy or the AlH^+ product, thereby determining whether this product ion would remain intact.

However, we were able to find a more efficient "short cut" to accurately (because our final cross-sections replicate most features of the experimental findings) estimate each trajectory's outcome. Briefly, we identified a reaction-path valley connecting the seam region discussed in the preceding paragraph to the $AlH^+ + H'$ products. The valley was found to be sloped steeply downhill along the lengthening Al−H′ distance and to display a potential "well" shape along the shorter (and nascently formed) Al−H distance. An example of these characteristics is shown below. We then *postulated* (this assumption being tested by verifying that our predicted product yields and cross-sections are in good agreement with what is seen experimentally) that flux crossing the seam and accessing this exit-channel valley would (a) proceed promptly down the steeply sloped direction of this valley with an initial velocity along the Al−H′ coordinate being that determined upon crossing the seam and (b) undergo vibrational motion along the Al−H coordinate with an initial kinetic energy, again determined by the velocity along this coordinate when the seam was crossed.

To effect the postulated model for treating the exit-channel dynamics, we first had to carefully characterize the steeply sloped valley and the shape of the potential along the transverse (Al−H) coordinate. Therefore, at 12 points along the seam denoted c in Figure 7, we first examined the behavior of the PES along a distortion in which one Al−H distance is shortened while the other Al−H′ distance is lengthened by the same amount, δ. The idea was to determine by how much the asymmetric distortion would occur spontaneously before the reactive PES would evolve into the exit-channel valley producing $AlH^+ + H'$.

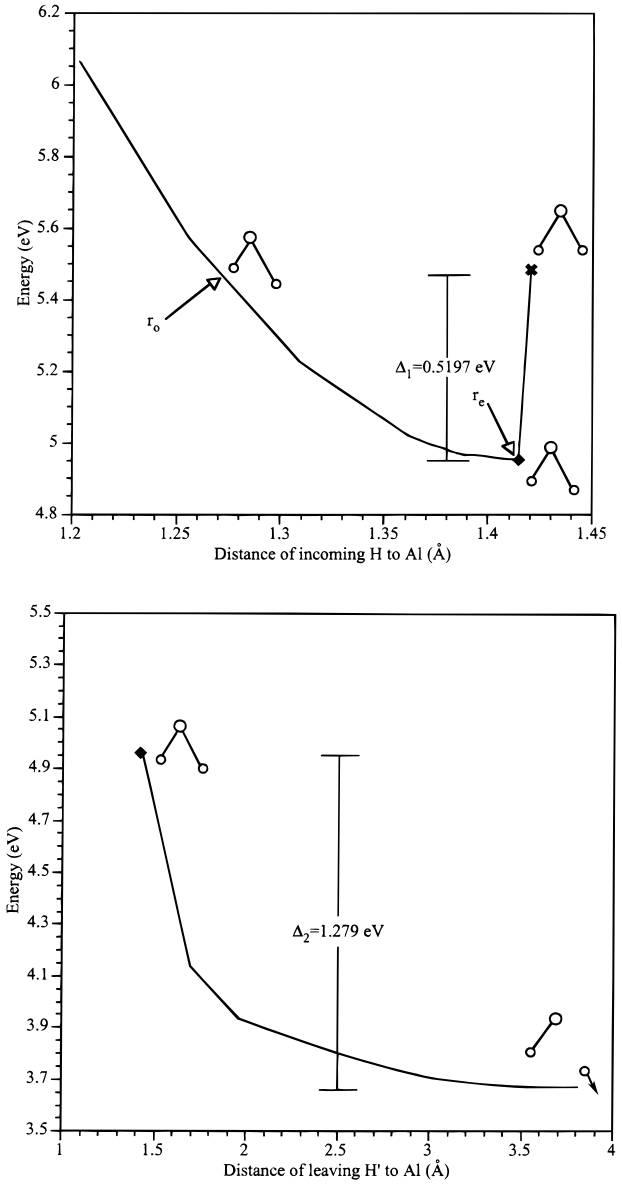

Figure 9. Energy versus Al to H distance as symmetry is broken upon crossing the seam c at the point 5 shown in Figure 7. (a) Shows how the potential energy changes as H is moved in by $\delta = 0.02$ Å along r_{AlH} and H′ is moved out by the same amount. **x** represents the last point on the $^1A_1$ potential surface where the b_2 mode is stable. ♦ marks the point r_e where the minimum energy is reached. r_o marks when the energy equals the energy at **x**, and Δ_1 is the maximum energy decrease. (b) Shows the result of fixing the r_{AlH} distance at r_e and increasing $r_{AlH'}$. ♦ is the corresponding point in a. Δ_2 is the energy decrease as H′ is pulled away.

For each of the 12 points just beyond (i.e., after crossing from the reactant side) the seam, the PES was found to display the type of behavior that is illustrated in Figure 9a for point no. 5 along the seam. A drop in energy (Δ_1) from the C_{2v} geometry accompanies the initial asymmetric distortion bringing the $AlHH'^+$ complex to a structure (characterized by a distance r_e to the nearest H atom) with unequal Al−H distances. Further compression of the shorter Al−H bond and symmetric lengthening of the other bond produces an increase in energy until the geometry r_0 (labeling the shorter bond length) is reached, where the energy is equal to its value prior to breaking C_{2v} symmetry. In Table 1 we list the values of the Δ_1, r_e, and r_0 parameters for the 12 representative points along the seam.

Beginning with each geometry characterized by its r_e, we next examined the gradient and local curvatures of the reactive PES. We observed that at each such geometry, the PES had a strong gradient along a direction in which the longer Al−H′ distance is increased while keeping the shorter Al−H distance (essentially) fixed at r_e; this is the steeply downhill direction discussed earlier. We, therefore, followed this gradient "downhill" from each of the 12 r_e geometries and examined how the energy evolved. In each case, the PES evolved downward to the energy of the $AlH^+ + H'$ asymptote. For the same point no. 5 used above as an example, Figure 9b shows how the energy decreases by an amount denoted Δ_2. In Table 1 are given the values of this Δ_2 energy fall off for a number of the 12 points along the seam.

TABLE 1: Minimum-Energy Bond Lengths r_e, Turning Points r_0, Energy Drops Δ_1 and Δ_2, and V_{Tess} for Points along Seam c Shown in Figure 7

point along seam	r_e (Å)	r_o (Å)	Δ_1 (eV)	Δ_2 (eV)	$V_{tess}(r,R)$ (eV)
1	1.24	1.24	0.00	2.678	8.11
2	1.29	1.28	0.00	2.267	7.02
3	1.336	1.241	0.326	1.856	6.30
4	1.366	1.307	0.354	1.644	5.86
5	1.414	1.254	0.520	1.279	5.47
6	1.424	1.291	0.495	1.178	5.32
9	1.545	1.333	0.490	0.912	4.81
11	1.597	1.334	0.495	0.808	4.66
12	1.622	1.357	0.538	0.737	4.58

4. How We Use the Exit-Channel PES Information. These probings of the PES from the seam region clearly show the PES displays a reaction valley (i.e., the locus of points each characterized by its r_e value that moves downhill by an amount Δ_2 as the Al−H′ coordinate increases) connecting each point along the seam to the $AlH^+ + H'$ products. In modeling the reaction using the classical trajectories, we made use of these data as follows:

(1) We compute the velocities along the Al−H and Al−H′ bonds as a trajectory crosses the seam (we actually use the nearby seam denoted b in Figure 7 because this seam characterizes where our entrance-channel PES remains valid before the bending force constant abruptly goes to zero). To account for the twisting potential energy (i.e., the geometry of the $AlHH'^+$ is likely not perfectly at a C_{2v} geometry) that is still present just as seam b is crossed, we compute (using the twisting potential-energy function discussed earlier) the changes in Al−H and Al−H′ velocities that will arise as this potential energy is released. This energy release generates (i) an outward change in velocity for the shorter Al−H bond and (ii) an inward change in velocity for the longer Al−H′ bond because the potential acts to restore C_{2v} symmetry. Combining the velocities that exist as the trajectory crosses the seam with these velocity increments provides our estimate of the instantaneous velocities as the actual seam c is crossed and the exit-channel valley is entered.

(2) We assume that the departing H′ atom will evolve, gaining kinetic energy along Al−H′ as the potential energy (Δ_2) is consumed, outward from the nascent $Al-H^+$ ion with no further influence on the molecular ion. This means that most of the energy release of the reaction will, if our model and its assumptions are correct, be carried off by the departing H′ atom (with a small recoil on the Al atom left behind).

(3) We use the above estimate of the velocity along the shorter Al−H bond to compute the kinetic energy T along this bond. We then use the length (r) of this Al−H bond as the seam was crossed, within a Morse-function approximation to the potential $V(r) = \Delta_1\{[1 - \exp(-\beta(r - r_e))]^2 - 1\}$, to compute the potential energy of the $Al-H'^+$ moiety. The Δ_1, r_e, and r_0 values of Table 1 are used for the point along the seam closest to where

the trajectory crossed to determine the Morse function with the β parameter being obtained as $\beta = (\ln 2)/(r_e - r_0)$.[17] Note that we use a Morse potential whose depth, equilibrium bond length, and curvature are obtained from the shape of the PES as the trajectory enters the exit-channel valley. As mentioned above, from this point on the departing H′ atom is assumed to have no further influence on the Al−H$^+$ ion.

(4) Finally, we determine whether the total energy along the Al−H coordinate, $T + V$, is less than the local dissociation energy Δ_1. If so, we count the trajectory as successful in forming the Al−H bond; if not, we say that the nascent AlH$^+$ dissociates and thus is not counted as contributing to our product cross-section.

B. Computed Cross-Sections vs Collision Energy. In parts a−c of Figure 10 are shown our final calculated reaction yield cross-sections as functions of the center of mass collision energy *E*. Although our threshold energies lie systematically below what is seen experimentally (due probably to a small error in the relative energy spacing between excited the $^1B_2$ and ground $^1A_1$ states and hence to small errors in the location of the "seam" region), they possess many of the attributes seen in the experimental data. In particular, (1) the cross-sections are much smaller than the gas-kinetic values and, in fact, have maxima that are within a factor of 2 of the experimental cross-sections (which is remarkable, in our opinion). The small cross-sections result primarily from the inefficiency in transferring collision energy into the H−H′ stretching coordinate. (2) The H_2 and D_2 thresholds are very nearly identical, as they are in the experimental data. (3) The energy gaps between the thresholds and peaks are ca. 2 eV for H_2, D_2, and AlD$^+$ from HD, as in the experiments. However, for AlH$^+$ from HD, our energy gap is also ca. 2 eV, while the experimental gap is nearly twice as large. (4) The Al$^+$ + HD → AlH$^+$ + D threshold is close to the thresholds for H_2 and D_2, as is the case in the laboratory data. (5) The Al$^+$ + HD → AlD$^+$ + H threshold is lower than the Al$^+$ + HD → AlH$^+$ + D threshold but not by as large an amount as that seen experimentally. The primary reason for this one threshold being lower than the other three seems to be that in the heteronuclear (HD) case, there is stronger coupling among the R', r, and θ' degrees of freedom (i.e., the potential $V(R, r, \theta)$ is more separable in the R, r, θ coordinates than in the R', r, θ' coordinates). (6) The overall shapes (i.e., steepness of onset, fall off at higher energy, and half widths at half-heights) are similar to what is seen experimentally except for the AlH$^+$ from HD case.

Because our simulated data replicates much of the experimental findings, we believe we have significant support for the quality of our potential-energy surface and the classical dynamics model we employed to compute trajectories on the tessellated surface and to define a reaction as occurring upon crossing of the seam of instability.

C. Trajectory Analysis. Although it is pleasing that our simulations give cross-sections in decent agreement with the guided-ion beam findings, it remains to explain *what causes the cross-sections to display these characteristics*. To arrive at a clear answer to this question, we examined a very large number of the reactive trajectories in the H_2, D_2, and HD cases. After a great deal of such effort, the following picture clearly arose: (1) Most collisions do not reach the seam region even though they may have enough energy to do so. These vast number of trajectories are nonreactive and account, in large part, for the small magnitude of the reaction cross-sections. That is, the peak magnitudes in the reactive cross-sections are determined by the efficiency with which collisional kinetic energy is converted to H−H′ stretching energy (as claimed in ref 5). (2) All trajectories reaching the seam have converted a significant amount of their collisional kinetic energy to the H−H′ stretching coordinate. That is, all points along the seam have extended H−H internuclear distances and thus significantly

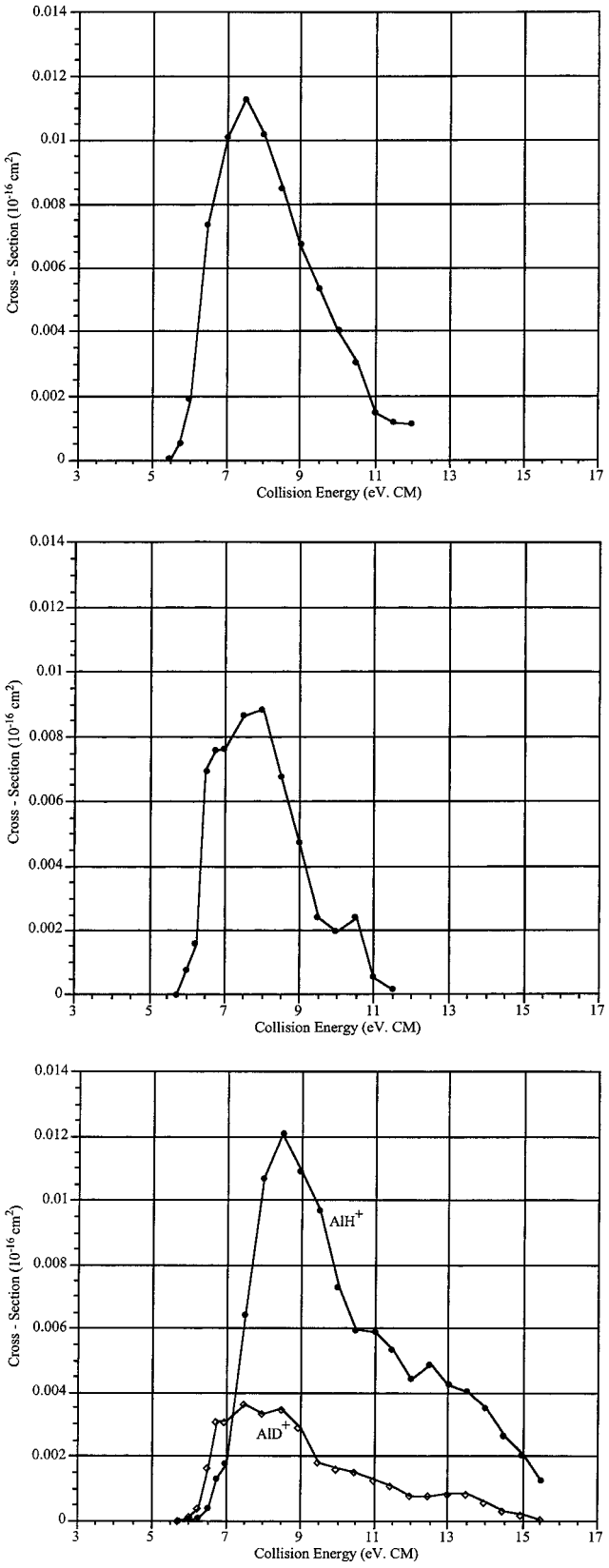

Figure 10. Cross-sections in cm^2 versus center of mass collision energy are in eV. (a) shows the results for Al$^+$ + H_2; (b) shows the results for Al$^+$ + D_2; (c) shows the results for Al$^+$ + HD.

TABLE 2: For Each Collision Energy, the Number and Percent of Reactive Trajectories with H or D Closest to Al^+

E_{coll} (eV)	no. of close Al to H	no. of close Al to D	% AlH	%AlD
5.75	0	2	0.00	100.0
6.00	0	46	0.00	100.0
6.50	0	255	0.00	100.0
7.00	11	427	2.51	97.49
7.50	53	774	6.41	93.59
8.00	90	925	8.87	91.13
8.50	103	1116	8.45	91.55
9.00	96	1321	6.77	93.23
9.50	79	1520	4.94	95.06
10.0	80	1639	4.65	95.35
10.5	83	1830	4.34	95.66
11.0	108	2057	4.99	95.01
11.5	158	2392	6.20	93.80
12.0	202	3418	5.58	94.42
12.5	167	2833	5.57	94.43
13.0	257	3985	6.06	93.94
13.5	360	4729	7.07	92.93
14.0	443	5250	7.78	92.22
14.5	527	5792	8.34	91.66
15.0	571	6297	8.31	91.69
15.5	613	6773	8.30	91.70

weakened H−H bonds. It is for this reason that the earlier[5] efforts connecting vibrational excitation probabilities to the reaction rates of these reactions met some success. (3) As the seam region is accessed for collision energies near or above threshold, both the Al−H and Al−H′ distances are near (close to thresholds) or shorter than (at higher collision energies) the equilibrium bond length in the product ion $Al-H^+$. (4) By the time trajectories cross the seam region, they have lost much of their kinetic energy. This energy has been absorbed by the repulsive potential energy of the ground-state surface. As a result, trajectories cross the seam with modest kinetic energies which we evaluate as described in section III.A.4 above. Much of the repulsive potential energy is, as the exit-channel valley is entered, released as kinetic energy of the departing H′ atom. (5) In essentially all reactive trajectories, the angular motion of the H−H′ molecule evolves from free rotation early in the trajectory at large R to oscillatory "rocking" motion as the Al^+ ion inserts into the H−H bond. Of course, the evolution of the free rotation to twisting motion is accompanied by a transfer of angular momentum from the H_2 to the AlH_2+ complex. (6) For HD, the geometry at which the angular twisting motion "locks in" has the Al^+ ion located over the center of mass of the H−D moiety (for H−H and D−D, this is the C_{2v} geometry), which causes the D atom to nearly always be closer to the Al^+ than the H atom as the seam is crossed.[18] To illustrate, in Figure 11a is shown the time evolutions of coordinates obtained at 10.0 eV CM collision energy for a trajectory that reaches the seam and reacts. These data illustrate how the HD rotates back to near C_{2v} symmetry as it approaches the seam and that, although the D atom is initially farther away from the Al^+, it ends up being closer as the seam is reached (see Figure 11b). Table 2 shows, among the reactive trajectories, the percentage of times for which D or H is closer to Al^+. At low collision energy, AlD^+ is more likely to form because D is closer and the AlD^+ will have low enough vibrational energy to remain bound. As E increases, the vibrational kinetic energy in the nascent AlD^+ ion becomes large enough to cause the AlD^+ to dissociate. However, at such collision energies where the AlD^+ is too energetic to remain stable, the $Al-H^+$ ion (which has a lower potential energy because the H atom is further from the Al^+ ion) may have low enough vibrational energy to remain stable. Hence, AlH^+ product ions begin to form as the AlD^+ product yield falls off. At even higher collision energies, the vibrational energy content of both $Al-H^+$ and $Al-D^+$ product ions exceeds Δ_1, so neither can be formed and remain stable enough to be detected. Therefore, both $Al-H^+$ and $Al-D^+$ cross-sections eventually fall off at high E.

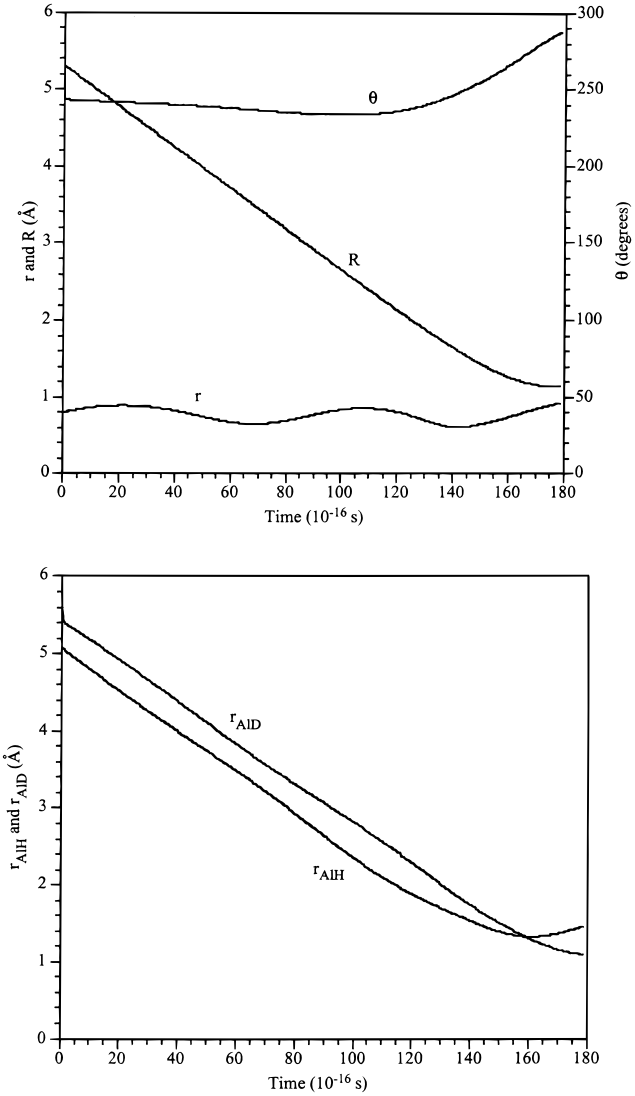

Figure 11. Representative reactive trajectory with a center of mass collision energy of 10.0 eV, impact parameter of 0.3 Å, and initial H−H bond distance of ca. 0.9 Å. (a) shows how the coordinates R, r, and θ evolve as a trajectory progresses along the entrance channel toward the seam; (b) Shows how the r_{AlD} and r_{AlH} distances change as time evolves.

IV. Summary

Our three-dimensional ab initio reactive energy surface, together with classical trajectory simulations of the $Al^+ + H_2 \rightarrow AlH^+ + H$ reactive collisions, produce cross-sections that display most of the features seen in the guided-ion beam data, although our thresholds are systematically lower than the experimental findings for reasons explained in section III.B.

Examination of a large number of reactive trajectories show a clear picture in which

(1) most collisions do not react because, due to inefficient transfer of collisional energy to H−H′ stretching, they do not access the "seam" region of the energy surface (this accounts for the small reactive cross-sections), (2) collisions are focused, by the shape of the potential-energy surface, away from collinear

and toward insertive geometries, (3) collisional kinetic energy is lost to repulsive potential energy and absorbed into the H−H′ stretching mode (thus weakening the H−H′ bond); this potential energy is eventually released as kinetic energy of the departing H′ atom, (4) a seam on the energy surface (where the restoring force maintaining near-C_{2v} geometry vanishes) is approached and crossed, (5) upon which a new Al−H$^+$ bond is formed preferentially between the Al$^+$ ion and the nearest H (or D) atom, after which (6) fragmentation to AlH$^+$ + H′ occurs.

These findings and the model this interpretation implies explain (1) the small magnitudes of the reactive cross-sections (i.e., few trajectories reach the seam), (2) the fact that all thresholds exceed the reaction endothermicity (the reaction cannot proceed along the collinear path that has no barrier but is forced to follow the insertive path to the seam region; the lowest energy point along the seam occurs at ca. 5 eV), (3) the small difference in the thresholds for H_2 and D_2 (the same place on the seam must be reached for both isotopes; n.b., the magnitudes of the H_2 and D_2 cross-sections are different reflecting different efficiencies in converting collisional kinetic energy into the H−H or D−D stretching mode), (4) the significant difference in AlD$^+$ and AlH$^+$ thresholds in the HD case (the Al$^+$ ion is almost always closer to the D atom, so bonding to the D atom occurs unless the kinetic energy along the Al−D coordinate is too high to allow the AlD$^+$ to be stable in which case AlH$^+$ bonding may occur), and (5) that at higher collision energies, the cross-sections fall off (the nascent AlH$^+$ or AlD$^+$ have too much vibrational energy to remain stable and thus dissociate).

Acknowledgment. This work was supported by NSF Grant No. CHE 9618904 and by proceeds from the Henry Eyring Chair. A grant of computer time from the Center for High Performance Computing is gratefully acknowledged.

References and Notes

(1) Armentrout, P. B. *Int. Rev. Phys. Chem.* **1990**, *9*, 115.

(2) Gutowski, M.; Roberson, M.; Rusho, J.; Nicholas, J.; Simons, J. *J. Chem Phys.* **1993**, *99*, 2601.

(3) O'Neal, D.; Taylor, H.; Simons, J. *J. Phys. Chem.* **1984**, *88*, 1510.

(4) Nichols, J.; Gutowski, M.; Cole, S.; Simons, J. *J. Phys. Chem.* **1992**, *96*, 644.

(5) Chacon-Taylor, M.; Simons, J. *Theor. Chim. Acta* **1995**, *90*, 357.

(6) Dunning, T. H. *J. Chem. Phys.* **1989**, *90*, 1007.

(7) McLean, A. D.; Chandler, G. S. *J. Chem. Phys.* **1980**, *72*, 5639.

(8) Schmidt, M. W.; Baldridge, K. K.; Boatz, J. A.; Elbert, S. T.; Gordon, M. S.; Jenson, J. H.; Koseki, S.; Matsunaga, N.; Nguyen, K. A.; Su, S.; Windus, T. L.; Dupuis, M.; Montgomery, J. A., Jr. *J. Comput. Chem.* **1993**, *14*, 1347.

(9) Moore, C. E. *Tables of Atomic Energy Levels*; Natl. Stand. Ref. Data Ser. **1971**, *35*/V.I.

(10) Salazar, M. R.; Bell, R. L. *J. Comput. Chem.* **1998**, *19*, 1431.

(11) Lawson, C. L. *Comput. Aided Geom. Des. J.* **1986**, *3*, 231.

(12) Alfeld, P. *Comput. Aided Geom. Des. J.* **1984**, *1*, 169.

(13) (a) It is known that this way of choosing initial r and R coordinates can give rise to artifactual oscillations in computed cross-sections, see: Bowman, J. M.; Kuppermann, A.; Schatz, G. C. *Chem. Phys. Lett.* **1973**, *19*, 20. However, it is unlikely that such problems have plagued our simulations given that we observe no unusual oscillations in the energy dependence of our cross-sections. (b) Bunker, D. L. *Theory of Elementary Gas Reaction Rates*; Pergmon Press: London, 1966.

(14) Simons, J. *Int. J. Quantum Chem.* **1993**, *48*, 211.

(15) Rusho, J.; Nichols, J. A.; Simons, J. *Int. J. Quantum Chem.* **1993**, *48*, 309.

(16) Simons, J. *Energetic Principles of Chemical Reactions*; Jones and Bartlett Publishers: Boston, 1983.

(17) To achieve the final cross-sections shown in the next section, we scaled the values of Δ_1 computed as described by a factor of 1.5. This factor of 1.5 was chosen because $1.5\Delta_1$ is close to the actual bond-dissociation energy ($D_e = 0.75$ eV) of AlH$^+$ for many of the points along the seam. If we use the unscaled Δ_1 values, the cross-sections are found to be only ca. 0.0015×10^{-16} cm^2 smaller.

(18) The result for HD may be surprising because the potential energy, which is identical for the three isotopes, has a minimum at $\theta = 90°$. However, there are also kinematic effects operative in the Al$^+$−HD kinetic energy (i.e., the kinetic energy is diagonal or uncoupled only when expressed in terms of the distance from Al$^+$ to the center of mass of H−D and the angle between the H−D internuclear axis and the vector connecting Al$^+$ to the HD center of mass). It is these kinetic-energy effects that cause the oscillation to occur not about the minimum of the potential but about a geometry in which the H−D axis is perpendicular to the vector connecting Al$^+$ to the center of mass of HD. Because the twisting occurs in this manner, the D atom is nearly always closer to the Al$^+$ ion than the H atom as the seam is crossed.